Journal of Zhejiang University-SCIENCE A (Applied Physics & Engineering) *2025 26(7):679-693*
www.jzus.zju.edu.cn; www.springer.com/journal/11582
E-mail: jzus_a@zju.edu.cn

Research Article

https://doi.org/10.1631/jzus.A2400431

Computational analysis of Ti-6Al-4V thoracic implants with a spring-like geometry for anterior chest wall reconstruction

Alejandro BOLAÑOS[1], Alejandro YÁNEZ[1]✉, Alberto CUADRADO[1], María Paula FIORUCCI[1], Belinda MENTADO[2,3]

[1]*Department of Mechanical Engineering, University of Las Palmas de Gran Canaria, Las Palmas de Gran Canaria 35017, Spain*
[2]*Department of Biomedical Engineering, Technological Institute of the Canary Islands (ITC), Arinaga 35118, Spain*
[3]*Osteobionix S.L, Santa Lucía de Tirajana 35118, Spain*

Abstract: Thoracic reconstructions are essential surgical techniques used to replace severely damaged tissues and restore protection to internal organs. In recent years, advancements in additive manufacturing have enabled the production of thoracic implants with complex geometries, offering more versatile performance. In this study, we investigated a design based on a spring-like geometry manufactured by laser powder bed fusion (LPBF), as proposed in earlier research. The biomechanical behavior of this design was analyzed using various isolated semi-ring-rib models at different levels of the rib cage. This approach enabled a comprehensive examination, leading to the proposal of several implant configurations that were incorporated into a 3D rib cage model with chest wall defects, to simulate different chest wall reconstruction scenarios. The results revealed that the implant design was too rigid for the second rib level, which therefore was excluded from the proposed implant configurations. In chest wall reconstruction simulations, the maximum stresses observed in all prostheses did not exceed 38% of the implant material's yield stress in the most unfavorable case. Additionally, all the implants showed flexibility compatible with the physiological movements of the human thorax.

Key words: Chest wall reconstruction; Thoracic implant; Spring-like geometry; Semi-ring-rib model; Computational analysis

1 Introduction

Chest wall reconstructions are surgical techniques aimed at restoring defects caused by the removal of specific portions of the thoracic cage. These techniques are necessary when primary tumors occur in the thoracic wall, soft tissues, bone, or cartilage, as well as following invasion of the thoracic wall by lung neoplasms (Kara et al., 2018). Regardless of the pathology being treated, the main objectives of all thoracic wall reconstructions are to recover dead space, restore the thoracic wall, mechanically preserve the lungs, protect intrathoracic organs, provide soft tissue coverage, minimize deformity, maintain an aesthetically acceptable appearance, and allow patients to undergo radiotherapy (Seder and Rocco, 2016). Currently, there is no consensus on standardized guidelines for thoracic wall reconstruction, although many surgeons recommend using these techniques for defects exceeding 5 cm or invasions affecting four or more ribs (Sanna et al., 2017). Different materials and techniques such as synthetic, biological, or titanium meshes, implants, and rigid titanium plates are also used in these interventions (Sanna et al., 2017).

Despite advances in the field of chest wall reconstruction, from 24% to 46% of patients experience postoperative problems associated with respiratory complications, among other causes (Hazel and Weyant, 2015). This occurs due to the use of reconstructive materials that are generally not flexible enough to allow lung inflation during the breathing process, which involves considerable rib movements and rotation angles produced by thoracic musculature (Luu et al., 2021). This substantial displacement of the rib cage leads to a prevalence of implant rupture in the anterior portion of the chest wall (Berthet et al., 2015).

✉ Alejandro YÁNEZ, alejandro.yanez@ulpgc.es
Alejandro BOLAÑOS, https://orcid.org/0009-0002-3426-7419
Alejandro YÁNEZ, https://orcid.org/0000-0002-1736-552X
Alberto CUADRADO, https://orcid.org/0000-0002-8599-781X
María Paula FIORUCCI, https://orcid.org/0000-0002-4532-7520

Received Sept. 2, 2024; Revision accepted Dec. 8, 2024;
Crosschecked May 27, 2025; Online first June 25, 2025

The development of new manufacturing techniques within additive manufacturing (AM) has allowed the fabrication of structures and geometric designs of greater complexity, resulting in prostheses with more versatile behavior, while having little impact on manufacturing time and enabling the production of fully customized devices (Kermavnar et al., 2021). Thanks to imaging through computerized tomography (CT), very precise 3D models of patients can be obtained using medical segmentation software, enabling the design to be adapted to suit each clinical case and printed using specific AM technologies.

Several studies have recently been conducted in this field, producing personalized thoracic implants. These prostheses use designs that replicate the shape of resected thoracic elements in a single piece (Wang et al., 2016; Wen et al., 2018) or even through modular designs (Aranda et al., 2019; Triviño et al., 2023). However, other studies (Aragón and Méndez, 2016; Moradiellos et al., 2017; Cano et al., 2018; Vannucci et al., 2020; Fiorucci et al., 2021; García et al., 2024) have gone further by using laser powder bed fusion (LPBF) manufacturing technology to obtain a design with a variable spring-like geometry that replaces the sternocostal complex, providing greater flexibility to accurately mimic the lengthening and shortening of costal cartilages during the breathing process. This new design concept has been used even in the manufacture of sternocostal implants (Kang et al., 2022) and costal cartilage prostheses (Zhang et al., 2020) using polyetheretherketone (PEEK) through fused deposition modeling (FDM) technology. However, this material has not been widely tested, and further analysis of its long-term biomechanical behavior is needed. This work represents a continuation of previous studies (Fiorucci et al., 2021) in which the behavior of this spring-like shape applied to the design of a thoracic implant was computationally studied in a specific semi-ring-rib model. Although the results obtained were promising, a more in-depth study of its biomechanical behavior and optimization was needed. Thus, the main objective of this work was to delve deeper into the study of this design. For this purpose, different implants were first studied in isolated semi-ring-rib models to assess their adaptability at different rib levels. Based on the results, various implant configurations were proposed and included in a more complex rib cage model with chest wall defects to study their biomechanical response in different simulated chest wall reconstruction scenarios. All models presented were tested using finite element (FE) software.

2 Materials and methods

2.1 Obtention and simulation conditions of individual semi-ring-rib models

First, four isolated rib models were used to analyze the individual responses of thoracic implants at various rib levels. To obtain the models, a CT scan (LightSpeed VCT, General Electric, USA) with a scanning interval of 0.6 mm was used to generate a digital imaging and communications in medicine (DICOM) file from the rib cage of a healthy 35-year-old adult man. This file was then imported into the commercial software Simpleware (Synopsys International Ltd., USA) to construct a 3D model, excluding the vertebral column, ligaments, thoracic muscles, and floating ribs for simplification. Only the bone structure and cartilaginous tissue were retained, including the first ten ribs with cortical and trabecular tissue, costal cartilages, and the sternum (Fig. 1). Finally, a parametric model was obtained by performing a symmetry operation in the mid-sagittal plane from the right hemithorax to avoid any asymmetry that could complicate the geometry and meshing of the model. The cortical thickness of all ribs was assumed to be 0.75 mm (Mohr et al., 2007).

Once the model was generated, ribs from the second to the fifth level of the rib cage were isolated, generating four individual semi-ring-rib models (Fig. 1). To analyze the behavior of the implants separately, the isolated ribs were resected and the implants were assembled. The first rib level was excluded because of the different biomechanical behavior of the ribs at this level, characterized by their shorter and stiffer shape, as well as the shorter length of the costal cartilage. The implants were designed with variable thickness (T) and width (W). The center had the dimensions T=2.5 mm and W=14 mm, continuously increasing until reaching the ends with T=2.7 mm and W=15 mm (Fiorucci et al., 2021). To adapt the implant design to the geometry of each rib, the centroid trajectory of each healthy rib was obtained and, following this trajectory, a folding pattern was introduced from the anterior face of the resected rib to the junction with the sternum, resulting in a cylindrical spring-like shape.

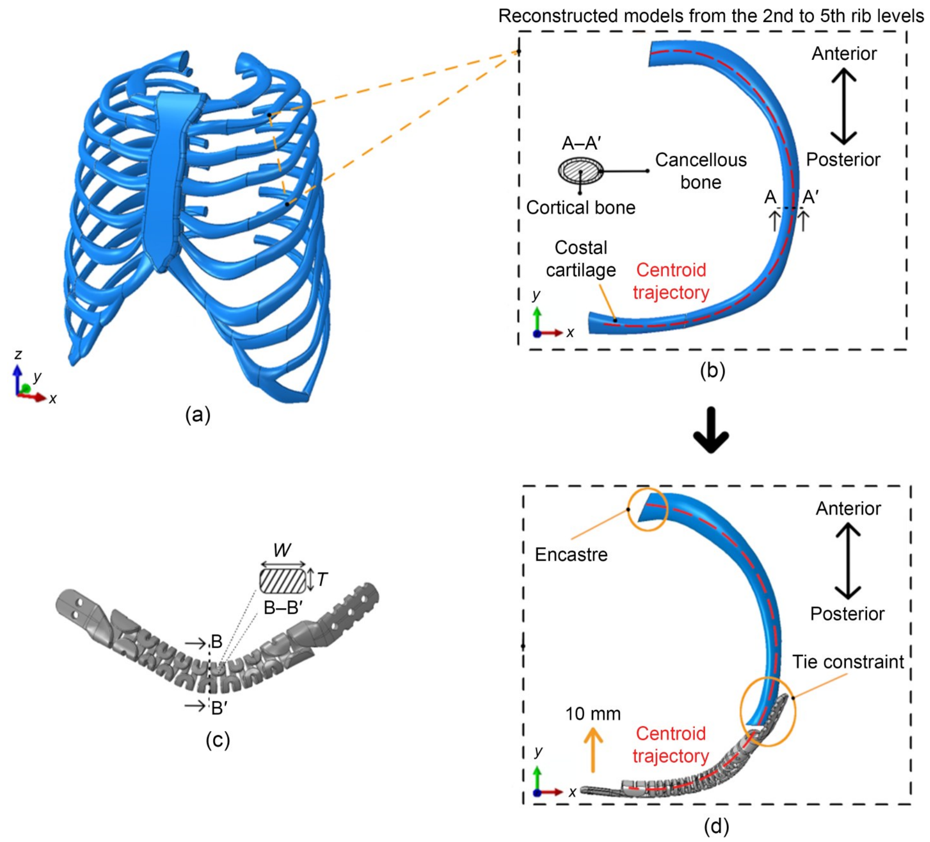

Fig. 1 Semi-ring-rib models obtained from the native model with the inclusion of implants from the second to the fifth rib level: (a) full rib cage model; (b) native semi-ring-rib model; (c) main design parameters of the implants; (d) reconstructed semi-ring-rib model

Each of the four isolated models was then imported into Abaqus software (Dassault System, SIMULIA Corp., USA) where all the necessary conditions for the FE study were defined. All materials were considered according to a linear elastic isotropic model, and mechanical properties were obtained from the scientific literature. The costal cartilage was assigned a Young's modulus of E=35.8 MPa and a Poisson's ratio of v=0.35 (Forman et al., 2010; Gradischar et al., 2022). The cortical bone was assigned E=14.4 GPa and v=0.30, and trabecular bone E=40.0 MPa and v=0.35 (Kemper et al., 2007; Li et al., 2010). Finally, the material characteristics applied to the implants (Ti-6Al-4V ELI (extra low interstitial) alloy) were defined by assigning E=110 GPa and v=0.30 (Yadroitsev et al., 2018; Yánez et al., 2022). A yield strength limit of S_y=869 MPa was also established for the plastic model (Rafi et al., 2013).

With respect to the boundary conditions, the posterior end of the rib was fixed. Considering that these models were analyzed in the xy plane, according to the reference system highlighted in Fig. 1, the only angle considered in this plane was the caliper angle, which develops around the z-axis. Since this angle is negligible compared to the pump handle angle, which occurs around the x-axis, and the bucket handle angle, associated with the y-axis, we decided to apply this fixation method to constrain all angles and displacements at the posterior end of the rib, to simplify the boundary conditions. Also, a 10-mm displacement (Li et al., 2010) was applied to the anterior end of the implant in the anteroposterior direction (y-axis) to simulate a simple bending deformation test (Fig. 1). This value was considered acceptable for simulating the compressive deformation of the sternum during the natural expiration process (Beyer et al., 2017). Finally, to compare the results, the same conditions were applied to the isolated semi-ring-rib models of healthy ribs, with the differences that the tie-type constraint was applied to the junction between the costal cartilage and the cortical bone, and the 10-mm displacement was applied to the anterior end of the costal cartilage.

Regarding the interaction between the elements, a tie constraint was established at the surfaces in contact between the implant and the cortical bone to prevent relative motion between them, and the posterior end of the rib was fixed, nullifying all displacements and rotations.

2.2 Validation of the native model of the full thorax

It was necessary to validate the behavior of the native model of the full thorax during the expiration process before studying its response to the thoracic implants. Therefore, the conditions necessary for the FE simulation were defined. Tie constraints were established in both costochondral and sternochondral joints to prevent relative movement between these elements. Regarding the boundary conditions summarized in Fig. 2, the displacement of all costovertebral joints along the three tridimensional axes was constrained to zero ($U_x=U_y=U_z=0$), along with the rotation around the z-axis (φ_z). The caliper angle was disregarded due to the small displacements experienced by the sternum in the laterolateral direction (de Groote et al., 1997). The angles for the laterolateral axis (φ_x), related to the x-axis, and the anteroposterior axis (φ_y), associated with the y-axis, were defined using coupling constraints linked to a reference point located at the center of the posterior end section of each rib, to simulate their connection to the vertebral column.

The values used to constrain the rotation angles on the x-axis and y-axis of each reference point were adjusted after testing different data, based on an analysis of how the external intercostal musculature functions during rib depression in the expiration process (Zhang et al., 2018; Zhao et al., 2022), and the kinematics of the costovertebral joint during the breathing cycle (Beyer et al., 2014). This testing was conducted in several simulations until we achieved a model response as realistic as possible compared to data from other studies (Gruben et al., 1999; Zhang et al., 2016; Sun et al., 2024). The values used for angle restriction at each rib level on both axes are summarized in Table 1.

Finally, various situations were considered according to criteria similar to those used by Sun et al. (2024) to validate the response of the model. First, its compressive behavior was analyzed during the natural chest compression process in the expiration phase of breathing, defining an anteroposterior displacement of 5 mm (de Groote et al., 1997) in the first seven costochondral joints to evaluate the pump handle and bucket handle angles generated in each rib during breathing (Fig. 2a). Then, different compressive loads were applied to the mid-sternum region to study the force–displacement curve of the model, considering the maximum anteroposterior sternal displacement and the respective compressive component of the applied force in each case (Fig. 2b). The load direction was always defined as being perpendicular to the sternal surface, and all loads were placed at the same point through a pin-type rigid solid constraint linked to the frontal surface of the sternum.

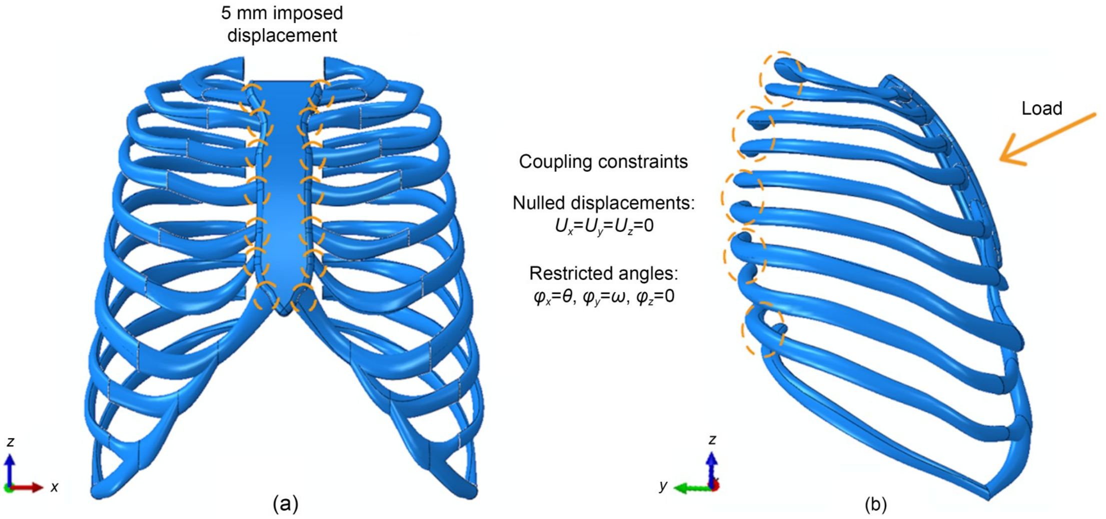

Fig. 2 Defined conditions for simulating the native model during the exhalation phase: (a) imposed displacement; (b) applied load and restrictions on the costovertebral joints. θ and ω refer to the values used to constrain the angles φ_x around the x-axis and φ_y associated with the y-axis, respectively, as summarized in Table 1 for each rib level

Table 1 Values used to constrain the angles in the laterolateral axis (φ_x) which occurs around the *x*-axis, and in the anteroposterior axis (φ_y) associated with the *y*-axis, at the costovertebral joints

Rib level	φ_x (°)	φ_y (°)
1	2.8	1.7
2	2.9	1.9
3	3.4	2.0
4	3.7	2.4
5	4.4	2.9
6	4.7	3.1
7	4.9	3.4
8	5.9	3.4
9	6.4	4.0
10	6.9	4.4

2.3 Obtention and simulation conditions of rib cage reconstruction models

With the aim of analyzing the behavior of the proposed spring-like design in a more realistic scenario of a chest wall defect, three different implant configurations were proposed. The aim was to address thoracic reconstructions under various conditions to reflect the variability of situations that can arise, from complex tumors that spread across both hemi-thoraxes (Aragón and Méndez, 2016) affecting bilateral thoracic structures, to locally invasive malignant neoplasms affecting unilateral tissues (Moradiellos et al., 2017; García et al., 2024). For this purpose, necessary elements of the native model were modified by resecting the third and fourth ipsilateral left ribs (model A1), the third, fourth, and fifth ipsilateral left ribs (model A2), and the third, fourth, and fifth bilateral ribs, as well as the affected portion of the sternum (model B), considering that the third, fourth, and fifth levels of ribs are frequently affected in thoracic resections (Weyant et al., 2006). Then, the corresponding prosthesis configuration was included in each case (Fig. 3).

Once each of the three models was modified and imported into the FE software, all restrictions and interactions between elements were defined as explained in Section 2.2, as well as material properties as described in Section 2.1. Additionally, a force of 300 N was applied at the same location on the sternum to simulate the action of a cardiopulmonary resuscitation (CPR) maneuver (Tomlinson et al., 2007) to study the response of the implants in an unfavorable scenario, given that this is a dangerous maneuver that under ordinary conditions may result in the fracture of healthy ribs if not applied correctly.

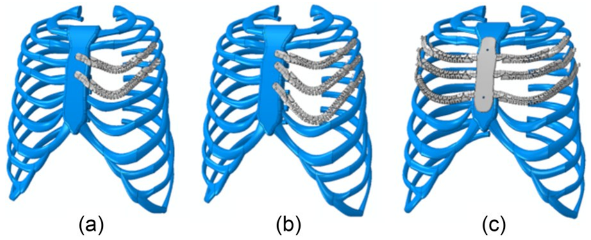

Fig. 3 Proposed implant configurations in this study: (a) reconstruction of the third and fourth left ipsilateral ribs (model A1); (b) reconstruction of the third, fourth, and fifth left ipsilateral ribs (model A2); (c) reconstruction of the third, fourth, and fifth bilateral ribs (model B)

Finally, all models were meshed with a quadratic mesh composed of ten-node tetrahedral elements (C_3D_{10}). A mesh sensitivity study was conducted after assigning element sizes of 1 or 2 mm to the models. For this study, model A1 was chosen as the reference model due to its lower complexity compared to the other models. The implant response was evaluated under a chest compression test with a load of 300 N under the same conditions as previously described.

3 Results

3.1 Mesh sensitivity study

The mesh sensitivity analysis showed that for the implant included in model A1, a maximum von Mises stress value of 316.5 MPa was obtained with the coarser mesh compared to 321.6 MPa for the finer mesh case (Fig. 4). Additionally, the average computational simulation time was 6 h versus 23 h, respectively, a difference of less than 2%. Thus, we chose to use the coarse mesh for all computational analyses due to its significantly lower computational cost.

3.2 Isolated semi-ring-rib models

After conducting computational tests on isolated rib models, the criterion of maximum principal stress was chosen to assess the results in the cortical tissue for each reconstructed semi-ring-rib model, as the behavior of human bone is not characteristic of a ductile material (Kemper et al., 2007; Palanca et al., 2022). Additionally, the maximum von Mises stress was obtained for each implant. At the third rib level, the

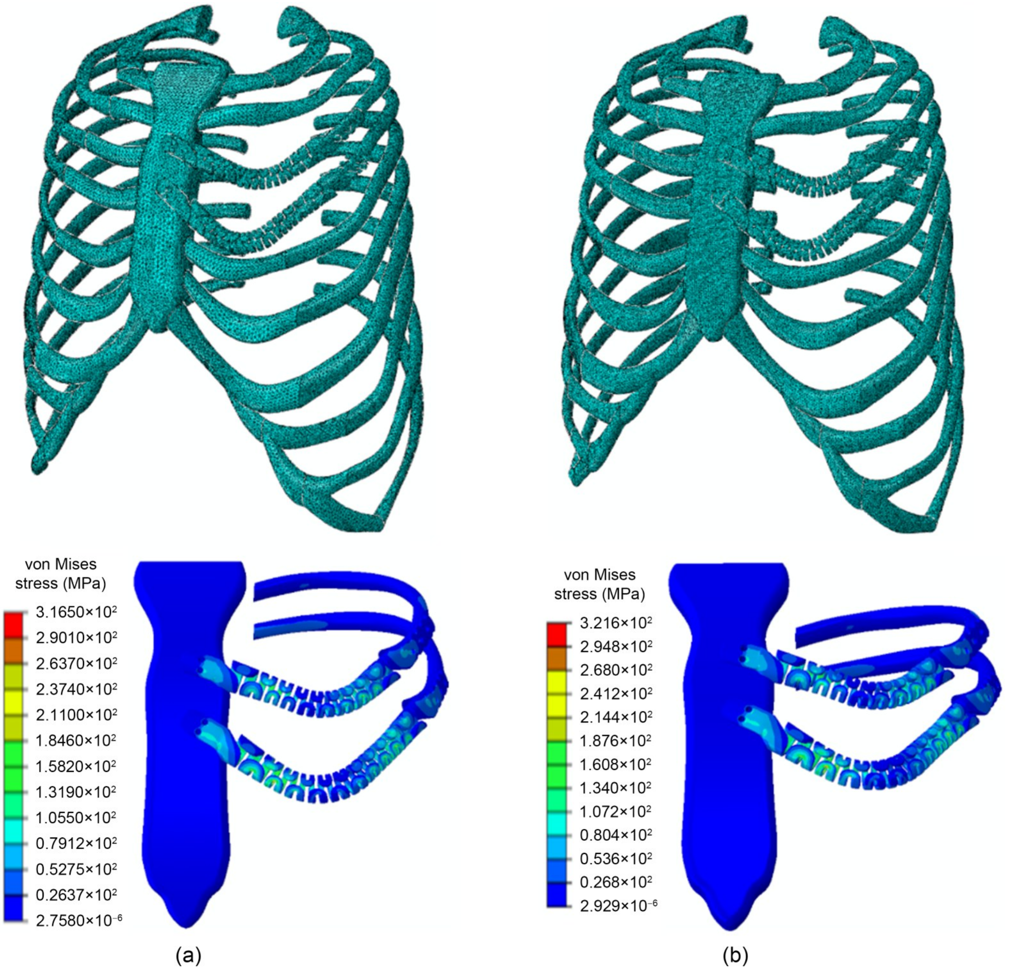

Fig. 4 von Mises stress result in the mesh sensitivity study: (a) coarse mesh (element size of 2 mm); (b) fine mesh (element size of 1 mm)

maximum principal stress in the cortical bone of the natural rib models was 30.0 MPa (Fig. 5a). In the reconstructed models, the maximum principal stress in the bone tissue reached 85.0 MPa at the second rib level, while the maximum von Mises equivalent stress in the implant was 237.2 MPa (Fig. 5b) at the same rib level. In all cases, it was observed that the maximum stresses in the bone were concentrated on the external lateral surface of the ribs.

The force–displacement curves of each of the four semi-ring-rib models reconstructed with implants were also obtained (Fig. 6). Their stiffness was calculated as the slope of the approximated lines, with a coefficient of determination (R^2) of 0.99 in all cases. The stiffness values calculated from the second to the fifth rib level were 6.1, 1.3, 0.7, and 0.4 N/mm, respectively. The stiffness obtained at the second rib level was more than four times higher than that at the third rib level.

3.3 Native model of the full thorax

During the expiration phase of the breathing cycle, the maximum sternal displacement was 10.3 mm in the anteroposterior direction and 17.8 mm in the laterolateral direction. Fig. 7 illustrates the distribution of displacements in the native model, along with the bucket handle angle and the pump handle angle generated in the ribs. Both angles were calculated using the method described by Wilson et al. (2001). Additionally, a comparison of these angles is shown with the results obtained in the computational models of Sun et al. (2024) and Zhang et al. (2016) for rib levels 2–7. Ribs at the first level and levels 8–10 were excluded from the visualization due to their different biomechanical behavior.

The highest absolute values obtained for the pump and bucket handle angles were 5.6° and 4.3°, respectively, at the seventh rib. Compared to the model of

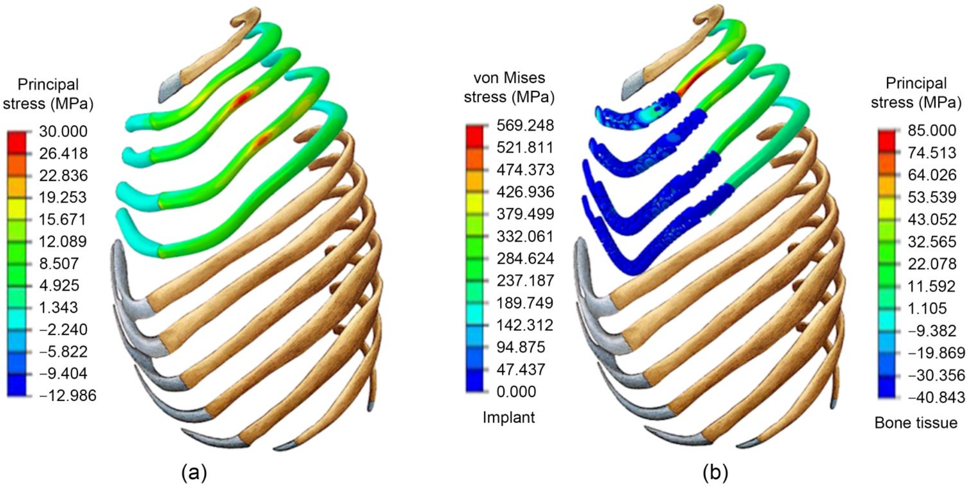

Fig. 5 Photographic composition showing the distribution of maximum principal stresses and the von Mises stresses in the cortical bone and in implants, respectively, of the isolated rib models from the second to the fifth rib level: (a) semi-ring-rib models with healthy ribs; (b) semi-ring-rib models reconstructed with implants (the left legend shows the results of the von Mises equivalent stresses obtained in the implant at each level, while the right legend presents the results obtained in the bone tissue)

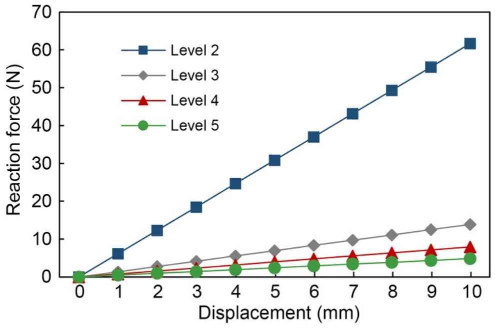

Fig. 6 Comparison of the force–displacement curves obtained for each of the four semi-ring-rib models reconstructed with implants

Zhang et al. (2016), the largest absolute differences observed were 1.7° at the fourth rib for the bucket handle angles and 1.3° at the seventh rib for the pump handle angles.

On the other hand, results obtained in the native model indicated that achieving a maximum sternal compression displacement of 30 mm required applying a force of about 340 N in its central zone. A force of 125 N was needed to produce a compression of 15 mm. Fig. 8 illustrates a comparison of the force–displacement curve of the native model in our study with those obtained by the models of Sun et al. (2024) and the experimental results from Gruben et al. (1999). The maximum relative differences observed in the maximum displacement estimates in these studies were 10.5% and 14.8%, respectively.

3.4 Chest wall reconstruction models

Compressive load simulations were conducted on models A1, A2, and B, resulting in von Mises stresses of 316.5, 295.8, and 327.5 MPa, respectively, in each implant. In all cases, these maximum stresses occurred in the anterior region near the junction with the sternum, with higher stresses observed in the areas of the prosthesis replacing the lowest rib, due to greater deformation of the sternum. Fig. 9 shows the stress distribution in each of the three implants, using the same scale.

Furthermore, the maximum compression displacement obtained in the sternum was 25.0 mm for model A1, 24.5 mm for model A2, and 20.1 mm for model B under the 300-N load scenario, compared to the 26.5 mm obtained in the case of the native model. Given that the coefficient R^2 was about 0.90 in all cases when evaluating the force–displacement curves, the stiffness of each was calculated as the slope of the line that best approximated them. The stiffness values obtained in each case are summarized in Fig. 10.

Finally, the total reaction force at each of the ten rib levels of the costovertebral joints was calculated as the sum of the resultant force from the anteroposterior (F_y) and craniocaudal (F_z) components of each pair of joints in each of the four models. The maximum reaction force occurred at the first level in all cases with minimal differences of around 3 N between the native

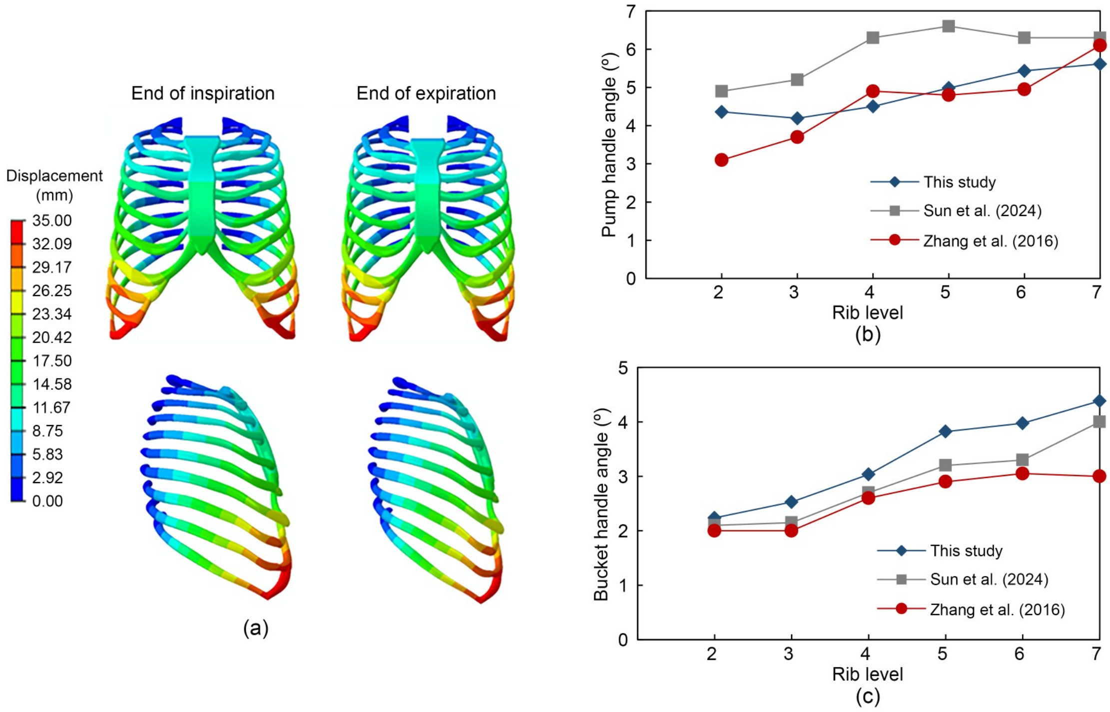

Fig. 7 (a) Total displacement of the native model from the final phase of the inspiration process to the final phase of the expiration movement shown above in coronal view and below in sagittal view (the scale factor applied was 1); (b) pump handle angle predicted in absolute value; (c) bucket handle angle predicted in absolute value

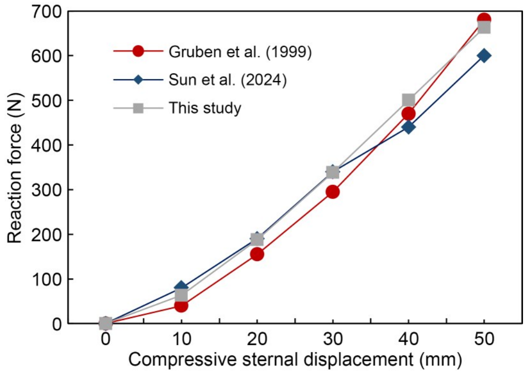

Fig. 8 Force–displacement curve of the native model compared with results obtained in other studies

model, model A1, and model A2. However, model B showed a greater difference, with the maximum reaction force being about 16.7 N lower than that of the native model (Table 2). Additionally, at rib levels 3, 4, and 5, model B exhibited the highest reaction forces compared to model A2, model A1, and the native model, with values of 48.1, 29.6, 29.5, and 22.9 N, respectively, at the third rib level.

The maximum principal stress values were obtained in model B, reaching 46.7 MPa. These stresses were located mainly at the anterior end of the resected ribs at the third rib level, displacing towards the costovertebral joint at the fourth and fifth rib levels (Fig. 11). At these levels, model B also showed the highest values of maximum principal stresses, with values of 43.2 and 41.7 MPa, respectively, compared to about 27.8 MPa in the native model.

4 Discussion

In this study, we evaluated the biomechanical behavior of thoracic implants with a spring-like design. Previous studies analyzed their response through experimental bending tests and computational simulations on a specific isolated rib model. Continuing from these studies, the response of implants from the second to the fifth levels of the thoracic cage was individually assessed in semi-ring-rib models. Analysis of results from this more comprehensive study led to the design of three implant configurations to be included in a complete rib cage model with chest wall defects. Thus, it was possible to study the biomechanical response of these implants in a more realistic scenario by simulating three different cases of chest wall reconstructions.

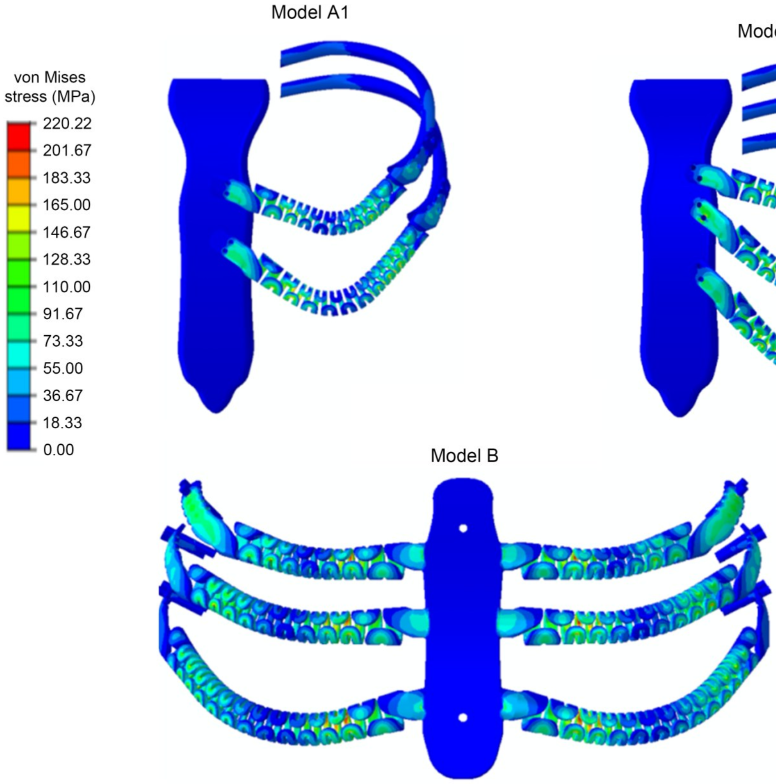

Fig. 9 Distribution of von Mises stresses in the implants for the three models. A maximum limit of 220 MPa was set in the representations to facilitate the comparison of the results obtained

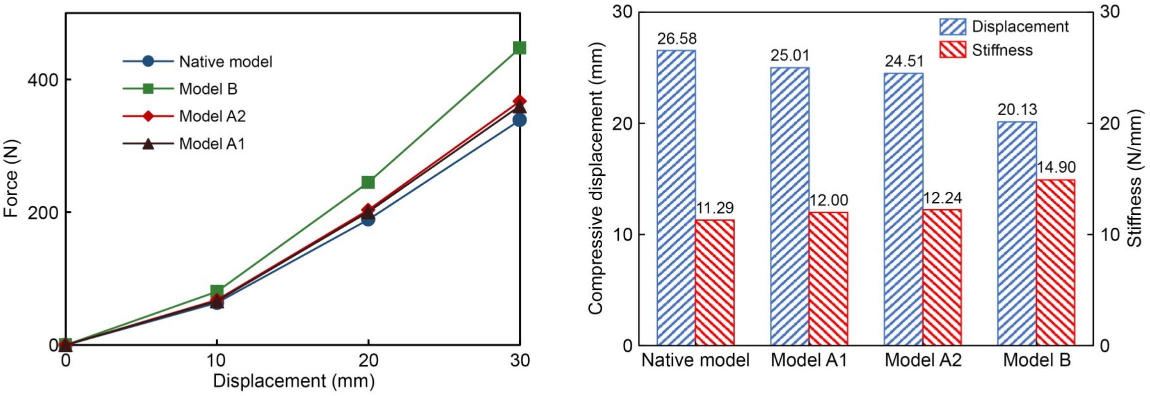

(a) (b)

Fig. 10 (a) Force–displacement curve obtained for each model; (b) comparison between the maximum compressive displacement in the sternum and the stiffness calculated for each model

After the simulations performed on the isolated semi-ring-rib models, the maximum principal stress in the cortical bone was 85 MPa at the second rib level but below 30 MPa at the remaining levels. Considering that the yield strength of cortical bone tissue can range between 88.0 and 100.7 MPa (Li et al., 2010; Iraeus et al., 2020), the design of the implant at the second level was considered excessively stiff due to the high stresses obtained in the cortical tissue, which could potentially harm the rib. Furthermore, the stiffness obtained from the implant-rib assembly was 6.1 N/mm, representing a 443% increase compared to the stiffness obtained at the third level. This increase could be attributed to the greater stiffness exhibited by the ribs at the second level, whose force–displacement curve was quite distinct from those of the other levels of the

Table 2 Results of reaction forces at each rib level in the four models presented

Rib level	Reaction force (N)			
	Native model	Model A1	Model A2	Model B
1	156.9	153.4	153.5	140.2
2	43.7	41.9	41.7	36.6
3	22.9	29.5	29.6	48.1
4	30.1	34.4	32.0	36.8
5	23.9	22.4	26.5	34.3
6	14.5	13.5	13.2	10.5
7	11.3	10.0	9.8	7.9
8	0.3	1.9	2.0	2.9
9	1.8	3.1	3.1	4.1
10	1.9	1.1	1.1	1.0

rib cage (Iraeus et al., 2020; Li et al., 2022). These results led to the design of three implant configurations for rib cage reconstruction, excluding the second rib level.

The next step involved validating the complete rib cage model before incorporating the proposed implant configurations to simulate different cases of chest wall reconstructions. This validation process included defining the necessary conditions within the FE software and analyzing the model's behavior under different conditions. The analysis included measuring the angles produced in the ribs during the natural compression process of the rib cage in the exhalation phase of breathing and examining the compression behavior of the model under the action of different compressive loads to obtain the corresponding force–displacement curve.

The results during the expiration phase of breathing were compared with those of more complex rib cage models that included a significant portion of the thoracic musculature (Zhang et al., 2016; Sun et al., 2024). The maximum absolute differences obtained in the pump handle angle compared to the models by Zhang et al. (2016) and Sun et al. (2024) were 1.2° at the second rib level and 1.7° at the fourth rib level. Similarly, for the bucket handle angle, these differences were 1.3° at the seventh level and 0.7° at the sixth level. The differences obtained could be a consequence of not including thoracic musculature, potentially leading to greater displacements in the ribs as they are solely linked to the boundary conditions of the model defined in the costovertebral joints. Nonetheless, although our proposed native model did not include any portion of the thoracic musculature, it showed significant consistency considering that in scientific literature, results with up to a 2° difference in these angles have been considered valid (Zhang et al., 2016; Zhao et al., 2022; Sun et al., 2024). Furthermore, the force–displacement curve of the model under different loading scenarios was compared with results from more complex computational models (Sun et al., 2024) and experimental data (Gruben et al., 1999). Although the response offered was more linear than in those studies, consistent results were obtained, considering that the relative difference calculated based on the maximum displacement difference in comparison with the results of those studies was less than 15%.

Although many studies have used complex models to simulate the breathing movements of the human chest as realistically as possible (Zhang et al., 2016; Zhao et al., 2022; Sun et al., 2024), this study has demonstrated that it is possible to use a simpler model and achieve realistic results. The lower complexity of the model is directly associated with a lower computational cost and, therefore, reduced time in executing simulations. It is important to consider that time is a key factor when designing and validating personalized prostheses for treating patients with serious clinical conditions. This allows for shorter response times and greater assurances in the implantation of prostheses.

Once the response of the native model was validated, different implant configurations were proposed to reconstruct the rib cage in various scenarios due to the great diversity of clinical cases that can be found (Aragón and Méndez, 2016; Moradiellos et al., 2017; Cano et al., 2018; Fiorucci et al., 2021). The three case studies for chest wall defects used in this study were chosen with the aim of forming a significant sample of possible cases, from reconstructions affecting ipsilateral ribs (models A1 and A2) to chest wall resections of bilateral structures (model B). The response of each configuration was studied in an unfavorable scenario during the practice of a CPR maneuver, applying an average load of 30 kg to the mid-sternum area. After conducting computational compressive tests, the maximum von Mises stress was reached in Model B with the bilateral prosthesis. In this case, this value was 327.5 MPa, a stress value that represents 38% of the yield stress value of the Ti-6Al-4V ELI alloy (Rafi et al., 2013). Considering this as the most unfavorable

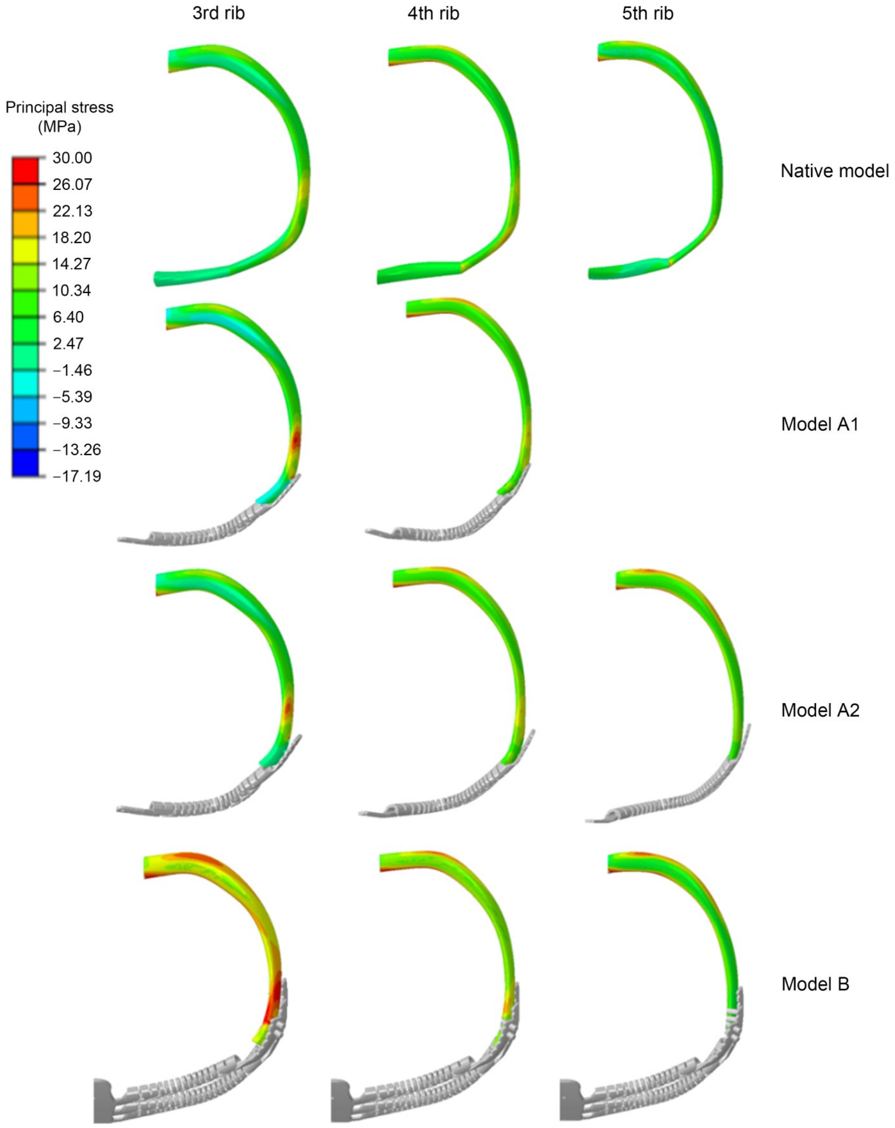

Fig. 11 Maximum principal stresses obtained in the bone tissue of the resected ribs for each of the four models in the third, fourth, and fifth left ribs. A maximum limit of 30 MPa was set to facilitate comparison, with all regions exceeding this threshold shown in intense red. References to color refer to the online version of this figure

case, we concluded that the proposed designs would withstand this situation without producing permanent deformations in the material.

Few studies have focused on analyzing the mechanical properties of implants manufactured through AM technologies (Fiorucci et al., 2021). Some studies have used semi-ring-rib models where the implant and the corresponding rib are isolated (Kang et al., 2018; Fiorucci et al., 2021) and a single deformation is applied in a unique coplanar direction, as also presented in the first part of this study. The inclusion of implants in our complete thoracic model has allowed for more precise results regarding the distribution of maximum principal stresses in the cortical bone, given that deformations are no longer generated solely in one plane, but considering the overall response of the 3D model. Consequently, maximum stresses are not only localized on the external lateral surface of the shaft of the ribs as obtained in the isolated rib models, but also concentrated on the external and internal posterior surfaces near the costovertebral joint, with this distribution differing according to each rib level.

Regarding the compressive displacements experienced by all models under the 300-N load scenario, a total stiffness of 11.2 N/mm was obtained for our native model. This value closely aligns with the findings from studies by Shaw et al. (2007) and Murach et al. (2018), where stiffness values of 12.8 and 13.0 N/mm, respectively, were found in compression tests on thoraxes from post-mortem eviscerated human subjects. The native model presented in this study consists uniquely of the bone structure and cartilaginous tissue of the rib cage, so the results obtained again demonstrated significant consistency with experimental data.

Models A1 and A2 showed a very similar response to that of the native model with minimal differences in maximum compression displacement, which was only 2 mm greater in models A1 and A2 and 5 mm in the case of model B. This may be attributed to the stiffness provided by the central plate's connection with the spring structure that replaces each of the costal cartilages, as well as the greater number of natural ribs replaced. Nevertheless, the research of Tomlinson et al. (2007) showed that some patients underwent compressive sternal displacements of less than 20 mm under a 30-kg load scenario. Thus, despite this increase in stiffness, the prosthesis included in model B appears to be compatible with the compression behavior of the human thorax. In addition, the average age of individuals included in the study of Tomlinson et al. (2007) was 70 years, while the native model presented in this work was derived from a healthy 35-year-old adult male. Therefore, the results are considered consistent given the reduction in stiffness experienced by the ribs over the years (Agnew et al., 2013, 2015).

Maximum principal stresses produced in the resected models were also analyzed. Table 2 shows the distribution of loads in the rib cage of each of the four models, resulting in an increase in the absorbed load at levels 3, 4, and 5 in models A1, A2, and B, where the resected ribs are located, and consequently, an increment in the maximum principal stresses produced on the bone tissue. The maximum stresses were located in the third level of ribs of model B, as expected, due to its higher stiffness, reaching a maximum value of 46.7 MPa. As mentioned previously, cortical bone yield stress values can range between 88.0 and 100.7 MPa at most (Li et al., 2010; Iraeus et al., 2020). Thus, the maximum stress produced in the cortical tissue represents about 53% of the lowest value of this interval in the most unfavorable case. Therefore, we conclude that stress distribution in healthy bone would not be detrimental under the analyzed scenario.

With regard to the load distribution of the rib cage after the reconstruction with the implants, the load absorption of the first two rib levels decreased compared to the native model, with these loads being redistributed to the ribs reconstructed with the implants. This behavior was also described in the study presented by Girotti et al. (2017), in which a rib cage prosthesis made of a polyester mesh and a rigid poly-methyl-methacrylate (PMME) structure was proposed. In that study, the model's response in all cases showed that over 60% of the applied load was absorbed by the first rib level due to the excessive stiffness of the prosthesis resulting from the absence of cartilaginous elements. In this study, the maximum percentage of absorption of load by the first rib level was less than 50% in all scenarios. This demonstrates that the spring structure used as the basis for the design of all implants allows for a reduction in the stiffness of the rib cage and a more precise replacement of costal cartilage elasticity, facilitating chest movements during breathing. This would result in a better quality of life for the patient, as described in previous cases (Aragón and Méndez, 2016; Moradiellos et al., 2017; Cano et al., 2018; Vannucci et al., 2020; García et al., 2024) where the new implant design was used. The clinical outcomes showed positive short-term results, ensuring a rapid recovery without severe complications or post-operative discomfort.

The model presented in this work consists of the bone structure and cartilaginous tissue of the thoracic cage only. The exclusion of the thoracic musculature has led to a less realistic response of the model in certain aspects compared to those documented in other studies. Future research analyzing the behavior of these implants in more demanding scenarios is necessary, especially regarding the long-term life of the implants. Rib movements during the natural breathing process generate cyclic loads that could facilitate the propagation of fissures in the material due to the layer-by-layer structure of parts produced by additive manufacturing (Yánez et al., 2020). In this regard, it is necessary to carry out research that further investigates the fatigue behavior of our proposed design. Specifically, low-cycle fatigue tests need to be conducted to study crack propagation in the geometry of the implants, while high-cycle fatigue analysis is necessary to determine whether these designs can withstand infinite life. Additionally, experimental tests are essential to further characterize the material properties related to fatigue performance, as well as to calibrate the computational models.

5 Conclusions

The thoracic implants proposed in this study have demonstrated adequate mechanical performance and flexibility when replacing the rib-cartilage complex, except for the second rib level where a high stiffness was obtained, resulting in a significant increase in cortical bone stresses. The specific spring-like geometry has yielded promising results in replacing the function of costal cartilage, enabling greater flexibility from the third to the fifth levels of the rib cage. Modifying certain design parameters could further reduce the stiffness of the implant, especially at the second rib level. In the three simulated scenarios of thoracic reconstructions, all tested designs endured mechanical stresses in demanding scenarios, induced acceptable stresses in the cortical tissue, and did not significantly alter the distribution of loads in the rib cage. Thus, the results obtained so far are promising, opening the door to the design of flexible, durable, and competitively produced custom-made implants.

Author contributions

Alejandro BOLAÑOS, Alejandro YÁNEZ, Alberto CUADRADO, and María Paula FIORUCCI designed the research. Belinda MENTADO collected the data. Alejandro BOLAÑOS processed the data and wrote the manuscript. Alejandro YÁNEZ, Alberto CUADRADO, María Paula FIORUCCI, and Belinda MENTADO helped to organize the manuscript. Alejandro YÁNEZ, Alberto CUADRADO, and María Paula FIORUCCI revised and edited the final version.

Conflict of interest

Alejandro BOLAÑOS, Alejandro YÁNEZ, Alberto CUADRADO, María Paula FIORUCCI, and Belinda MENTADO declare that they have no conflict of interest.

References

Agnew AM, Kang YS, Moorhouse K, et al., 2013. Age-related changes in stiffness in human ribs. Proceedings of the IRCOBI Conference, p.257-269.

Agnew AM, Schafman M, Moorhouse K, et al., 2015. The effect of age on the structural properties of human ribs. *Journal of the Mechanical Behavior of Biomedical Materials*, 41:302-314. https://doi.org/10.1016/j.jmbbm.2014.09.002

Aragón J, Méndez IP, 2016. Dynamic 3D printed titanium copy prosthesis: a novel design for large chest wall resection and reconstruction. *Journal of Thoracic Disease*, 8(6):E385-E389. https://doi.org/10.21037/jtd.2016.03.94

Aranda JL, Novoa N, Jiménez MF, 2019. Thoracic customized modular titanium-printed prosthesis. *AME Case Reports*, 3:35. https://doi.org/10.21037/acr.2019.08.01

Berthet JP, Gomez Caro A, Solovei L, et al., 2015. Titanium implant failure after chest wall osteosynthesis. *The Annals of Thoracic Surgery*, 99(6):1945-1952. https://doi.org/10.1016/j.athoracsur.2015.02.040

Beyer B, Sholukha V, Dugailly PM, et al., 2014. In vivo thorax 3D modelling from costovertebral joint complex kinematics. *Clinical Biomechanics*, 29(4):434-438. https://doi.org/10.1016/j.clinbiomech.2014.01.007

Beyer B, Feipel V, Sholukha V, et al., 2017. In-vivo analysis of sternal angle, sternal and sternocostal kinematics in supine humans during breathing. *Journal of Biomechanics*, 64:32-40. https://doi.org/10.1016/j.jbiomech.2017.08.026

Cano JR, Escobar FH, Alonso DP, et al., 2018. Reconstruction of the anterior chest wall with a 3-dimensionally printed biodynamic prosthesis. *The Journal of Thoracic and Cardiovascular Surgery*, 155(1):E59-E60. https://doi.org/10.1016/j.jtcvs.2017.08.118

de Groote A, Wantier M, Cheron G, et al., 1997. Chest wall motion during tidal breathing. *Journal of Applied Physiology*, 83(5):1531-1537. https://doi.org/10.1152/jappl.1997.83.5.1531

Fiorucci MP, Cuadrado A, Yánez A, et al., 2021. Biomechanical characterization of custom-made dynamic implants fabricated by electron beam melting for anterior chest wall reconstruction. *Materials & Design*, 206:109758. https://doi.org/10.1016/j.matdes.2021.109758

Forman JL, de Dios EDP, Kent RW, 2010. A pseudo-elastic effective material property representation of the costal cartilage for use in finite element models of the whole human body. *Traffic Injury Prevention*, 11(6):613-622. https://doi.org/10.1080/15389588.2010.517254

García JRC, Shao ML, Monopoli D, 2024. Giant reconstruction of right hemithorax with 3D custom dynamic prosthesis. *Archivos de Bronconeumología*, 60(3):177-178. https://doi.org/10.1016/j.arbres.2023.12.015

Girotti A, Rosa F, Ferrotto M, et al., 2017. Mechanical behavior of a total chest wall prosthesis with rib-like features. *Computer Methods in Biomechanics and Biomedical Engineering*, 20(15):1581-1588. https://doi.org/10.1080/10255842.2017.1391952

Gradischar A, Lebschy C, Krach W, et al., 2022. Measurement of global mechanical properties of human thorax: costal cartilage. *Journal of Biomechanics*, 142:111242. https://doi.org/10.1016/j.jbiomech.2022.111242

Gruben KG, Halperin HR, Popel AS, et al., 1999. Canine sternal force-displacement relationship during cardiopulmonary resuscitation. *IEEE Transactions on Biomedical Engineering*, 46(7):788-796.

https://doi.org/10.1109/10.771188

Hazel K, Weyant MJ, 2015. Chest wall resection and reconstruction: management of complications. *Thoracic Surgery Clinics*, 25(4):517-521. https://doi.org/10.1016/j.thorsurg.2015.07.013

Iraeus J, Brolin K, Pipkorn B, 2020. Generic finite element models of human ribs, developed and validated for stiffness and strain prediction–to be used in rib fracture risk evaluation for the human population in vehicle crashes. *Journal of the Mechanical Behavior of Biomedical Materials*, 106:103742. https://doi.org/10.1016/j.jmbbm.2020.103742

Kang JF, Wang L, Yang CC, et al., 2018. Custom design and biomechanical analysis of 3D-printed PEEK rib prostheses. *Biomechanics and Modeling in Mechanobiology*, 17(4): 1083-1092. https://doi.org/10.1007/s10237-018-1015-x

Kang JF, Tian YC, Zheng JB, et al., 2022. Functional design and biomechanical evaluation of 3D printing PEEK flexible implant for chest wall reconstruction. *Computer Methods and Programs in Biomedicine*, 225:107105. https://doi.org/10.1016/j.cmpb.2022.107105

Kara HV, Keenan JE, Balderson SS, et al., 2018. Video assisted thoracic surgery with chest wall resection. *Video-Assisted Thoracic Surgery*, 3(4):15. https://doi.org/10.21037/vats.2018.03.07

Kemper AR, McNally C, Pullins CA, et al., 2007. The biomechanics of human ribs: material and structural properties from dynamic tension and bending tests. Proceedings of the 51st Stapp Car Crash Conference, p.235-273.

Kermavnar T, Shannon A, O'Sullivan KJ, et al., 2021. Three-dimensional printing of medical devices used directly to treat patients: a systematic review. *3D Printing and Additive Manufacturing*, 8(6):366-408. https://doi.org/10.1089/3dp.2020.0324

Li Z, Subit D, Kindig MW, et al., 2022. Development of a finite element ribcage model of the 50th percentile male with variable rib cortical thickness. Proceedings of the 38th International Workshop of Injury Biomechanics Research.

Li ZP, Kindig MW, Kerrigan JR, et al., 2010. Rib fractures under anterior-posterior dynamic loads: experimental and finite-element study. *Journal of Biomechanics*, 43(2): 228-234. https://doi.org/10.1016/j.jbiomech.2009.08.040

Luu BL, McDonald RJ, Bolsterlee B, et al., 2021. Movement of the ribs in supine humans for small and large changes in lung volume. *Journal of Applied Physiology*, 131(1): 174-183. https://doi.org/10.1152/japplphysiol.01046.2020

Mohr M, Abrams E, Engel C, et al., 2007. Geometry of human ribs pertinent to orthopedic chest-wall reconstruction. *Journal of Biomechanics*, 40(6):1310-1317. https://doi.org/10.1016/j.jbiomech.2006.05.017

Moradiellos J, Amor S, Córdoba M, et al., 2017. Functional chest wall reconstruction with a biomechanical three-dimensionally printed implant. *The Annals of Thoracic Surgery*, 103(4):E389-E391. https://doi.org/10.1016/j.athoracsur.2016.11.048

Murach MM, Kang YS, Bolte JH, et al., 2018. Quantification of skeletal and soft tissue contributions to thoracic response in a dynamic frontal loading scenario. *Stapp Car Crash Journal*, 62:193-269.

Palanca M, Liebsch C, Hübner S, et al., 2022. Global and local characterization explains the different mechanisms of failure of the human ribs. *Journal of the Mechanical Behavior of Biomedical Materials*, 125:104931. https://doi.org/10.1016/j.jmbbm.2021.104931

Rafi HK, Karthik NV, Gong HJ, et al., 2013. Microstructures and mechanical properties of Ti6Al4V parts fabricated by selective laser melting and electron beam melting. *Journal of Materials Engineering and Performance*, 22(12): 3872-3883. https://doi.org/10.1007/s11665-013-0658-0

Sanna S, Brandolini J, Pardolesi A, et al., 2017. Materials and techniques in chest wall reconstruction: a review. *Journal of Visualized Surgery*, 3(7):95. https://doi.org/10.21037/jovs.2017.06.10

Seder CW, Rocco G, 2016. Chest wall reconstruction after extended resection. *Journal of Thoracic Disease*, 8(S11): S863-S871. https://doi.org/10.21037/jtd.2016.11.07

Shaw G, Lessley D, Evans J, et al., 2007. Quasi-static and dynamic thoracic loading tests: cadaveric torsos. Proceedings of the International IRCOBI Conference on the Biomechanics of Impact, p.325-348.

Sun CN, Dong EC, Tian YC, et al., 2024. Functional biomimetic design of 3D printed polyether-ether-ketone flexible chest wall reconstruction implants for restoration of the respiration. *Materials & Design*, 237:112574. https://doi.org/10.1016/j.matdes.2023.112574

Tomlinson AE, Nysaether J, Kramer-Johansen J, et al., 2007. Compression force–depth relationship during out-of-hospital cardiopulmonary resuscitation. *Resuscitation*, 72(3):364-370. https://doi.org/10.1016/j.resuscitation.2006.07.017

Triviño A, López-Cano R, Machuca J, 2023. Chondrosarcoma of manubrium: innovative chest wall reconstruction. *Archivos de Bronconeumología*, 59(4):251-252. https://doi.org/10.1016/j.arbres.2022.11.006

Vannucci J, Scarnecchia E, Potenza R, et al., 2020. Dynamic titanium prosthesis based on 3D-printed replica for chest wall resection and reconstruction. *Translational Lung Cancer Research*, 9(5):2027-2032. https://doi.org/10.21037/tlcr-20-699

Wang L, Cao TS, Li XF, et al., 2016. Three-dimensional printing titanium ribs for complex reconstruction after extensive posterolateral chest wall resection in lung cancer. *The Journal of Thoracic and Cardiovascular Surgery*, 152(1): E5-E7. https://doi.org/10.1016/j.jtcvs.2016.02.064

Wen XP, Gao S, Feng JT, et al., 2018. Chest-wall reconstruction with a customized titanium-alloy prosthesis fabricated by 3D printing and rapid prototyping. *Journal of Cardiothoracic Surgery*, 13(1):4. https://doi.org/10.1186/s13019-017-0692-3

Weyant MJ, Bains MS, Venkatraman E, et al., 2006. Results of chest wall resection and reconstruction with and without

rigid prosthesis. *The Annals of Thoracic Surgery*, 81(1): 279-285.
https://doi.org/10.1016/j.athoracsur.2005.07.001

Wilson TA, Legrand A, Gevenois PA, et al., 2001. Respiratory effects of the external and internal intercostal muscles in humans. *The Journal of Physiology*, 530(2):319-330.
https://doi.org/10.1111/j.1469-7793.2001.0319l.x

Yadroitsev I, Krakhmalev P, Yadroitsava I, et al., 2018. Qualification of Ti6Al4V ELI alloy produced by laser powder bed fusion for biomedical applications. *JOM*, 70(3):372-377.
https://doi.org/10.1007/s11837-017-2655-5

Yánez A, Fiorucci MP, Cuadrado A, et al., 2020. Surface roughness effects on the fatigue behaviour of gyroid cellular structures obtained by additive manufacturing. *International Journal of Fatigue*, 138:105702.
https://doi.org/10.1016/j.ijfatigue.2020.105702

Yánez A, Fiorucci MP, Martel O, et al., 2022. The influence of dimensions and powder recycling on the roughness and mechanical properties of Ti-6Al-4V parts fabricated by laser powder bed fusion. *Materials*, 15(16):5787.
https://doi.org/10.3390/ma15165787

Zhang CG, Wang L, Kang JF, et al., 2020. Bionic design and verification of 3D printed PEEK costal cartilage prosthesis. *Journal of the Mechanical Behavior of Biomedical Materials*, 103:103561.
https://doi.org/10.1016/j.jmbbm.2019.103561

Zhang GZ, Chen X, Ohgi J, et al., 2016. Biomechanical simulation of thorax deformation using finite element approach. *BioMedical Engineering Online*, 15(1):18.
https://doi.org/10.1186/s12938-016-0132-y

Zhang GZ, Chen X, Ohgi J, et al., 2018. Effect of intercostal muscle contraction on rib motion in humans studied by finite element analysis. *Journal of Applied Physiology*, 125(4):1165-1170.
https://doi.org/10.1152/japplphysiol.00995.2017

Zhao XL, Guo SJ, Xiao S, et al., 2022. Thorax dynamic modeling and biomechanical analysis of chest breathing in supine lying position. *Journal of Biomechanical Engineering*, 144(10):101004.
https://doi.org/10.1115/1.4054346